

Highly efficient narrow bandgap Cu(In,Ga)Se₂ solar cells with enhanced open circuit voltage for tandem application

Received: 9 May 2024

Accepted: 19 November 2024

Published online: 28 November 2024



Junjun Zhang¹, Zengyang Ma¹, Yitian Zhang¹, Xinxing Liu¹, Ruiming Li¹, Qianqian Lin¹, Guojia Fang¹, Xue Zheng², Weimin Li², Chunlei Yang², Jianmin Li¹, Junbo Gong¹✉ & Xudong Xiao¹✉

Although an ideal bandgap matching with 0.96 eV and 1.62 eV for a double-junction tandem is hard to realize practically, among all mature photovoltaic systems, Cu(In,Ga)Se₂ (CIGSe) can provide the closest bandgap of 1.00 eV for the bottom sub-cell by adjusting its composition. However, pure CuInSe₂ (CISE) solar cell suffers strong interfacial carrier recombination. We hereby present approaches to introduce appropriate Ga gradients in both the back and front parts of absorber while maintaining the absorption spectrum close to CISE. With an appropriate front Ga gradient, the open circuit voltage can be enhanced by ~30 mV. With a pre-deposited CIGSe layer and a high copper excess deposition during absorber growth, the Ga diffusion can be well suppressed and a wide U-shaped Ga grading with a minimum bandgap of 1.01 eV has been created. Our optimized narrow-bandgap CIGSe solar cell has achieved a certified record PCE of 20.26%, with a record-low open circuit voltage deficit of 368 mV and a record-high contribution of 10% absolute efficiency to a four-terminal tandem. This work demonstrates the potential of controlling gallium diffusion to improve the performance of narrow bandgap CIGSe solar cells for tandem applications.

Tandem solar cells have recently emerged as a research forefront due to their potential to practically surpass the inherent Shockley-Queisser efficiency limit in single-junction solar cells¹. By integrating multi-subcells with different energy bandgaps, tandem solar cells aim to enhance the utilization of the solar spectrum^{2,3}. Theoretically, the best bandgap combination for a double-junction tandem system is determined as 0.96 eV for bottom subcell and 1.62 eV for top subcell, potentially yielding a power conversion efficiency (PCE) of 46.1% under one-sun radiation under ideal conditions^{2,4}. In the recent studies, the widely employed top subcell is the wide bandgap perovskite solar cells, while the popular choices for the bottom subcells include Si (E_g ~ 1.12 eV), Cu(In,Ga)Se₂ (CIGSe, E_g ~ 1.00–1.68 eV), and narrow bandgap perovskite (E_g ~ 1.20 eV) solar cells^{5–14}. Among these, CIGSe

stands out, as it can be fabricated with a minimum bandgap of 1.00 eV, showcasing the optimal potential to approach the theoretical PCE. Inspired by the success of conventional bandgap Cu(In,Ga)(S,Se)₂ (CIGSSe) solar cells that have already achieved a PCE of 23.35% and (Ag,Cu)(In,Ga)Se₂ solar cells that present a record efficiency of 23.64%^{15,16}, the investigation into narrow bandgap CIGSe solar cells has recently emerged as an active and promising topic of research^{17–20}.

At present, the PCE of narrow bandgap CIGSe solar cells remains relatively low. The natural choice of the narrowest bandgap CIGSe is pure CuInSe₂ (CISE, E_g ~ 1.00 eV) without alloying any Ga in the light absorber. The best PCE achieved for such solar cells is 15.0%²¹, primarily limited by its small open circuit voltage (V_{oc}) originating from a large recombination at both the front and back interfaces^{22,23}.

¹School of Physics and Technology, and Key Laboratory of Artificial Micro- and Nano-structures of Ministry of Education, Wuhan University, Wuhan 430072, China. ²Shenzhen Institute of Advanced Technology, Chinese Academy of Sciences, Shenzhen 518055, China. ✉e-mail: gongjunbo@whu.edu.cn; xdxiao@whu.edu.cn

Recognizing that the aforementioned energy bandgap matching requirement in tandems must be more precisely stated as a requirement on the absorption-spectral matching of the subcells, the bandgap of the light absorbers can be structured, as long as the absorption of the appropriate solar spectrum is maintained. In this spirit, a single Ga grading was introduced at the back of light absorber in order to reduce the back interface recombination of CIGSe²². Coupled with higher Cu composition and RbF post-deposition treatment (PDT) to improve the bulk and the front surface quality, a V_{OC} of 609 mV and a PCE of 19.2% were reached for a bandgap-graded CIGSe^{24,25}. This single Ga back-grading exemplifies a strategy that engineers the bandgap structure of the light absorber while maintaining the spectral absorption identical to pure CIGSe²⁴.

To further promote the PCE of narrow bandgap CIGSe solar cells, a crucial avenue involves the elevation of V_{OC} . In the above optimal CIGSe device with a 1.00 eV bandgap, the short circuit current density (J_{SC}) and the fill factor (FF) have reached 87.76% and 87.15%, respectively, of their respective Shockley-Quiesser limit (48.2 mA/cm² and 85.6%)²⁶. However, the V_{OC} lags significantly at 79.61% of its Shockley-Quiesser limit (765 mV), far behind the other two performance parameters. Considering the established efficacy of Ga front grading in enhancing the V_{OC} of normal bandgap CIGSe²⁷, we hereby propose a double-Ga-grading strategy for engineering the narrow bandgap CIGSe in both back and front parts of the absorber (Supplementary Fig. 1), aiming to further boost the V_{OC} . Unfortunately, at high growth temperature, the inter-diffusion between Ga and In elements poses a challenge, practically smearing the Ga grading and leading to an increased minimum bandgap in CIGSe (Supplementary Fig. 1)^{20,28}, thus limiting the absorption of the infrared light of solar spectrum. Therefore, the principal challenge in the double-Ga-grading approach for forming narrow bandgap CIGSe is to precisely control the inter-diffusion between Ga and In elements at nanoscales while maintaining spectral absorption as close to CIGSe as possible.

We have applied three key stages of nanoscale control to cooperatively achieve the above goal in the present experimental work. In the first and second stages of control, a front Ga grading within the p-n junction region via evaporating Ga at the very end of absorber layer growth and a steep back Ga grading via depositing a pre-CIGSe layer

with high Ga content were respectively introduced (Fig. 1b) to effectively suppress the Ga and In inter-diffusion and enable an increase of V_{OC} by ~40 mV after adjusting the bandgap change. In the third stage of control, a 15% excessive Cu deposition after the stoichiometric point ($[Cu]/([Ga] + [In])$ (CGI) = 1 at this point) during absorber growth was employed to not only increase grain size and reduce defect density, improving carrier transport and enhancing optical absorption, but further limit Ga and In inter-diffusion due to reduced Ga_{Cu} and In_{Cu} antisites. With these three stages of nanoscale control, we have successfully fabricated a narrow bandgap absorber with an optimized U-shaped double Ga grading that possesses a notch as wide as 0.90 μm and a bandgap as narrow as 1.01 eV. This narrow bandgap CIGSe absorber in the device structured as Glass/Mo/CIGSe/CdS/i-ZnO/AZO/MgF₂ has enabled a solar cell with a V_{OC} of 642 mV, a J_{SC} of 41.70 mA/cm², an FF of 76.06%, and a PCE of 20.37% (certified PCE of 20.26% with V_{OC} = 637 mV, J_{SC} = 41.62 mA/cm², FF = 76.44%), which is the highest reported efficiency for narrow bandgap CIGSe. Paired with a wide bandgap perovskite top cell, this CIGSe bottom cell makes a contribution of 10% absolute efficiency, surpassing all existing reports, in a four-terminal tandem configuration.

Results

Raising V_{OC} by controlling the Ga front grading

Up to today, the low V_{OC} stands as the primary limitation in narrow bandgap CIGSe devices although a few research groups have demonstrated that Ga back grading is an effective method for enhancing the efficiency of narrow-bandgap CIGSe solar cells^{23,24,29}. In order to investigate the possibility of double Ga grading in narrow bandgap solar cells and the impact of Ga content near the front interface of CIGSe on device performance and V_{OC} , four groups of CIGSe absorbers with different amounts of Ga added in the third stage of deposition process were fabricated, as shown in Fig. 1b. The deposition sequences prior to the third stage were kept the same as follows: First, a high Ga content CIGSe layer (see next subsection) was grown on soda lime glass with a Mo back contact, then the standard In+Se and Cu+Se deposition processes in the first and second stages were followed. Afterwards, in addition to In deposition, the amount of Ga in the third stage was varied to control the Ga front grading. We here use FG-0, FG-5, FG-10, and FG-20 to represent samples with varying amounts of

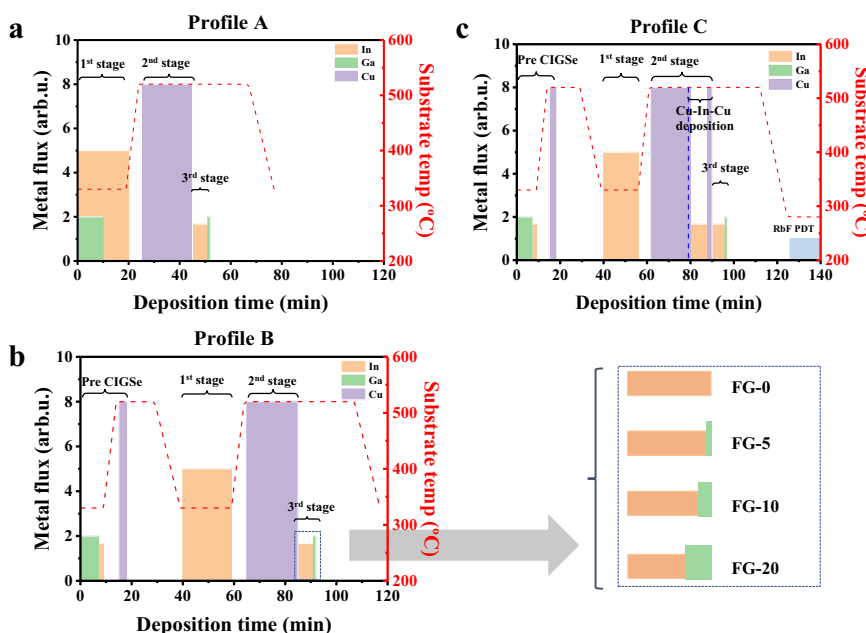


Fig. 1 | Schematic of deposition sequence for different profiles. a Schematic of growth sequence of profile A based on normal “three stage” deposition. **b** Schematic of growth sequence of profile B with a pre-CIGSe layer and different Ga content in

the 3rd stage. **c** Schematic of growth sequence of profile C with excessive Cu deposited in the second stage.

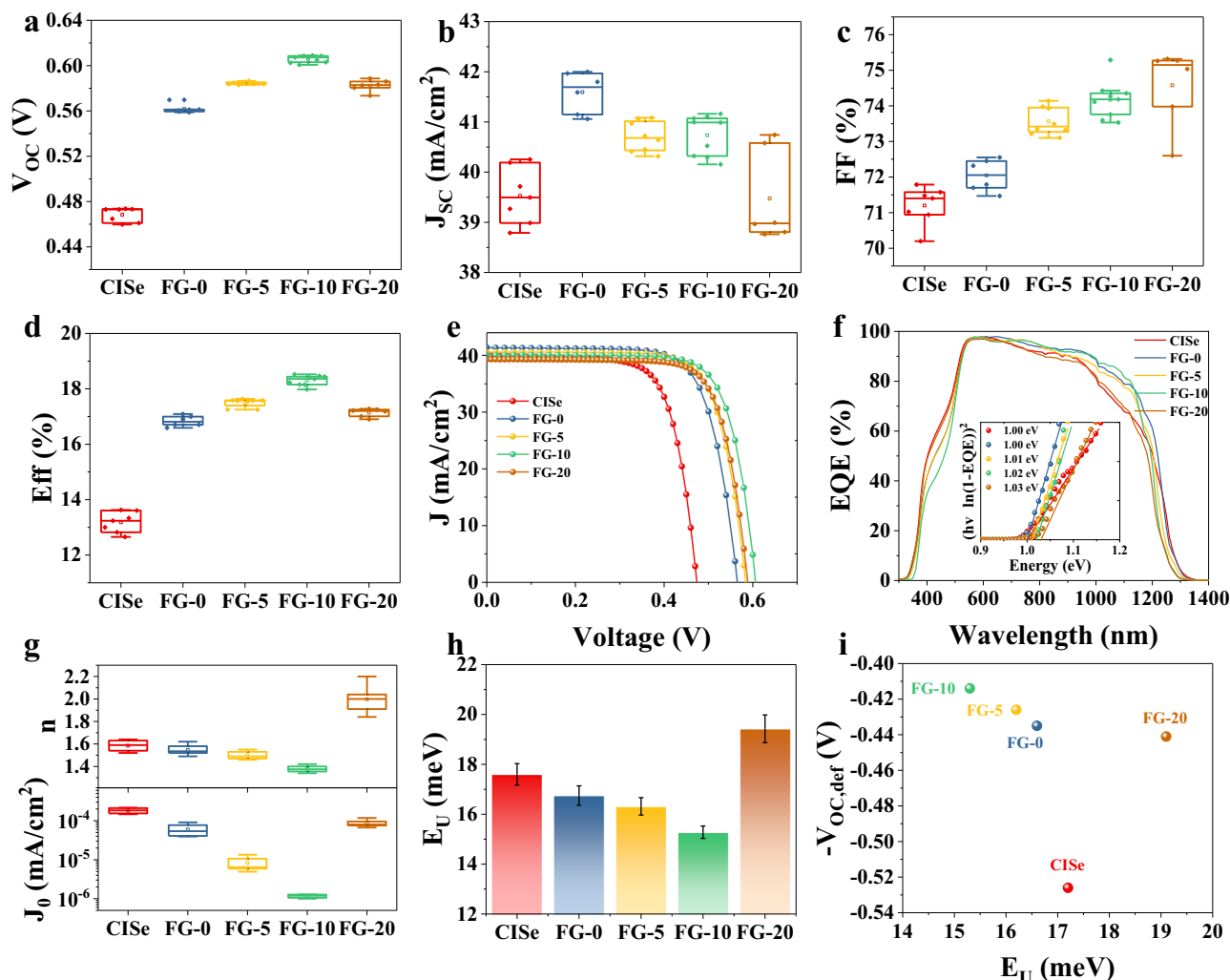


Fig. 2 | Effects of Ga front grading on device performance. **a–d** Statistical boxplot of (a) V_{OC} , (b) J_{SC} , (c) FF , (d) Eff of different groups of CIGSe solar cells (about 6–8 cells in each group). **e, f** Typical J - V curves and EQE spectra of the corresponding CIGSe solar cells. **g** J_0 and n with statistical error bars determined from 4 to 6 devices in each group of narrow bandgap CIGSe solar cells with different Ga

content supplied in the third stage. **h** Bar plot of Urbach energy with error bars determined from 4 to 6 devices in each group. **i** $-V_{OC,def}$ as a function of E_U for four different CIGSe solar cells. For a complete comparison, our results of pure CIGSe solar cells are also included in all the panels.

Ga introduced in the third stage to from the front Ga grading, respectively corresponding to 0%, 5%, 10%, and 20% of the Ga content in the pre-CIGSe layer.

The PV performance parameters and the typical J - V and EQE curves of the devices with various front Ga gradients are shown in Fig. 2a–f. Due to the absence of Ga and the relatively lower bandgap at the front surface, Sample FG-0 exhibits a high J_{SC} of 41.6 ± 0.4 mA/cm² with a bandgap of 1.00 eV, while its FF and V_{OC} are notably lower than the other devices. The introduction of a front Ga grading significantly improves the V_{OC} compared to the single bandgap grading CIGSe solar cells. By adjusting the Ga content in the third stage to an optimal amount (FG-10), as compared to the FG-0 solar cells, an enhancement of -44 mV in V_{OC} and -2.8% absolute in FF has been achieved. However, the diffusion of Ga into the notch region has unfortunately increased the minimum bandgap of the absorber from 1.00 eV to 1.02 eV, leading to a J_{SC} loss of -1 mA/cm². After adjustment of the bandgap change by the Shockley-Queisser limit²⁶, a net V_{OC} increase of -30 mV can be attributed to the introduction of front bandgap grading, leading to an improvement of PCE from -16.8% to -18.3%. Nevertheless, further increase of Ga in the third stage (FG-20) unfortunately would not only increase the minimum bandgap but also reduce V_{OC} .

Supplementary Fig. 2 depicts the dark J - V curves and the $\ln(EQE)$ curves of various CIGSe solar cells: CIGSe, FG-0, FG-5, FG-10, and FG-20. The deduced diode parameters are plotted in Fig. 2g and listed in Table 1. As the Ga content increases in the third stage, both the reverse saturation current (J_0) and the ideality factor (n) exhibit a trend of initial decrease and then an increase, demonstrating that the optimization is reached at the Ga content of -10% (FG-10), for which the device exhibits the lowest J_0 ($(1.16 \pm 0.13) \times 10^{-6}$ mA/cm²) and n (1.38 ± 0.03). These results suggest that introducing an appropriate amount of Ga in the third stage of deposition process can effectively reduce the carrier recombination in the p-n junction and at the front interface^{30,31}.

The Urbach energy (E_U) for the four different samples is determined by fitting an exponential curve to the EQE data in the sub-bandgap region (Supplementary Fig. 2b) and plotted in Fig. 2h. Fig. i presents the corresponding relationship between the E_U and the open-circuit voltage deficit ($V_{OC,def}$). A positive correlation is observed between the values of E_U and $V_{OC,def}$. Sample FG-10 achieves the highest PCE and exhibits the lowest values of E_U and $V_{OC,def}$. This correlation aligns well with observations in various types of thin-film solar cells previously studied³². The aforementioned results clearly demonstrate

Table 1 | Photovoltaic parameters of the narrow bandgap CIGSe solar cells with different Ga content supplied in the third stage

Sample	V_{OC} (mV)	J_{SC} (mA/cm ²)	FF (%)	η (%)	n	J_0 (mA/cm ²)	E_U (mV)	E_g (eV)	$V_{OC,def}$ (V)
ClSe	468 ± 6	39.5 ± 0.6	71.2 ± 0.5	13.2 ± 0.4	1.59 ± 0.06	$1.83 \pm 0.33 \times 10^{-4}$	17.60 ± 0.43	1.00	0.532 ± 0.006
FG-0	562 ± 4	41.6 ± 0.4	72.0 ± 0.4	16.8 ± 0.2	1.55 ± 0.05	$5.93 \pm 2.05 \times 10^{-5}$	16.75 ± 0.39	1.00	0.438 ± 0.004
FG-5	584 ± 2	40.7 ± 0.3	73.6 ± 0.4	17.6 ± 0.2	1.50 ± 0.04	$8.25 \pm 3.60 \times 10^{-6}$	16.32 ± 0.35	1.01	0.426 ± 0.002
FG-10	606 ± 3	40.7 ± 0.4	74.2 ± 0.5	18.3 ± 0.2	1.38 ± 0.03	$1.16 \pm 0.13 \times 10^{-6}$	15.28 ± 0.25	1.02	0.414 ± 0.003
FG-20	582 ± 5	39.5 ± 1.0	74.6 ± 1.1	17.1 ± 0.2	2.00 ± 0.14	$8.71 \pm 2.01 \times 10^{-5}$	19.42 ± 0.56	1.03	0.448 ± 0.005

that a substantial improvement of V_{OC} can be achieved with minimal compromise to the minimum bandgap of CIGSe.

Steepening the back Ga grading via pre-formed high Ga content CIGSe layer

In order to maintain the minimum bandgap as close to that of ClSe as possible for optimal utilization of solar spectrum, we must carefully suppress the Ga diffusion from the back part of absorber into the ClSe region (notch region). Three different samples based on the deposition profiles illustrated in Fig. 1a, b were fabricated to control the slope of back Ga grading towards the Mo back contact. With Profile A shown in Fig. 1a, Sample A was grown by first evaporating Ga and In simultaneously for approximately 10 min onto a Mo-coated substrate at 330 °C, and then depositing pure In for another 10 min. In the second stage, Cu was deposited at a high substrate temperature of 520 °C until a slight Cu-rich phase was achieved. In the third stage, In was deposited first, followed by deposition of 10% Ga of that in the first stage so that the CGI composition reached to a value of -0.92. Sample B1 and B2 were both grown with Profile B shown in Fig. 1b, which introduced a pre-CIGSe layer with 80% Ga and 20% In to achieve a steeper back Ga grading. To investigate the effect of the pre-CIGSe layer thickness on the performance of narrow bandgap CIGSe devices, Sample B1 used 430 nm thick pre-CIGSe and Sample B2 used 20% thinner pre-CIGSe. To ensure high crystalline quality, this pre-CIGSe layer was subsequently annealed at high temperature for 10 min in Se atmosphere. Afterwards, the substrate temperature was cooled back to 330 °C and the normal “three stage” deposition process similar to Profile A was applied by depositing only pure In in the first stage. The total thickness of the CIGSe absorbers was maintained the same for all samples through In deposition. In all three samples, Ga deposited in the third stage was -10% of the first stage or of the pre-CIGSe as optimized previously.

The steepened back Ga grading can affect the V_{OC} as well as the J_{SC} . As shown in Fig. 3, the corresponding cross-sectional scanning electron microscopic (SEM) images and GGI ([Ga]/([Ga]+[In])) depth profiles for the absorbers are demonstrated. For better visual effect, the three-dimensional mappings of Ga and In elements from Time-of-Flight Secondary Ion Mass Spectrometry (ToF-SIMS) are also included. While Sample A exhibits slightly larger grains, Sample B1 and B2 have smaller but similar grain sizes, possibly due to a larger Ga content near the back interface. Because of the stronger inter-diffusion between In and Ga in Sample A than in Sample B1 and B2, as displayed in the GGI distribution in Fig. 3b and visualized in the spatial ToF-SIMS mapping of Ga element (Fig. 3c, d), the resulted Ga back grading decreases from GGI - 0.22 at the back interface to -0.04 at the minimum of the notch for Sample A. With the front Ga grading deposited, a V-like grading is formed with a notch width of -0.40 μm (region with GGI ≤ 0.01+minimum GGI) despite the deliberate front-loading of Ga in the first stage (Fig. 1a). Even modifying Profile A by evaporating Ga first and In latter with no overlapping period, in principle ensuring the largest possible Ga back grading in its class (Supplementary Fig. 3), the SIMS results clearly demonstrate that the GGI distribution changes mainly near the Mo back contact with negligible effect to widen the notch region. With the introduction of a high Ga content pre-CIGSe layer in Sample B1 and B2, a steeper back Ga grading is achieved. The slope of

the back GGI grading is -1.5 times that in Sample A, leading to a decrease from GGI - 0.25 at the back interface to -0.03 at the minimum of the notch for Sample B1, and a decrease from GGI - 0.24 at the back interface to -0.02 at the minimum of the notch for Sample B2. The wider notch in Sample B1 (~0.54 μm) than that in Sample A (~0.40 μm) results in a more U-like GGI distribution that is advantageous for absorbing the infrared light to increase J_{SC} by -1.0 mA/cm² to 40.40 mA/cm². The further lowered GGI minimum for Sample B2 results in narrower bandgap and a more broadened notch region of -0.75 μm and an increased J_{SC} to 41.40 mA/cm² (Table 2 and Fig. 4b). Despite of the measurement uncertainty, the increase in J_{SC} is also observable from the EQE spectra (Fig. 4f), from which a better spectral response is observed for Sample B1 than for Sample A in the 950–1100 nm range due to a widened notch width, and for Sample B2 than for Sample B1 above -1150 nm due to the slightly narrowed bandgap. As shown in the inset of Fig. 4f, the introduction of pre-CIGSe layer to the narrow bandgap CIGSe absorber lowers the minimum optical bandgap from 1.03 eV for sample A to 1.02 eV for sample B1 and to 1.01 eV for Sample B2. Surprisingly, in spite of their similar overall Ga content, the steeper back Ga grading for Sample B1 against Sample A leads to a noticeable improvement of V_{OC} by -10 mV, increased from 601 mV of Sample A to 614 mV of Sample B1 in contrast to their minimum bandgap values. Further, despite of the lowered minimum bandgap by -0.02 eV for Sample B2 compared to Sample A, their V_{OC} remains similar. These results reveal that the steeper back Ga grading can increase the V_{OC} in addition to J_{SC} ³³. Such steepened Ga grading leads to both a larger GGI height difference and a larger GGI slope, with the former to expel electrons from the back interface by a large effective potential and the latter by a large effective field, both of which reduce the back interface recombination^{16,33}.

It is worth noting that annealing the pre-CIGSe layer is beneficial for the CIGSe device performance. Optimizing this annealing time to 600 s can result in an improvement of V_{OC} by -10 mV and of FF close to 1% absolute (Supplementary Fig. 4), possibly due to variations in the inter-diffusion between In and Ga that results from the differences in the crystalline quality of the pre-CIGSe layer. Such differences are also noted between Sample B1 and Sample FG-10. Although both of them used nominally the same growth conditions, without annealing the pre-CIGSe layer leads the latter to somewhat lower efficiency. As further demonstrated in the SEM images of Sample B1 and B2 (Fig. 3a), no discernible deterioration of the crystalline morphology is observed in the overall CIGSe absorbers grown with the high Ga content pre-CIGSe layer. Consequently, Sample B1 shows an overall enhancement against Sample A in device performance, including V_{OC} , J_{SC} , and FF (Fig. 4a–d), with the median efficiency increased to 18.93% from 17.82%. Even with a reduction of the overall GGI, which leads to a decreased V_{OC} and FF but an increased J_{SC} due to the narrower bandgap, Sample B2 demonstrates only a slightly lowered median efficiency to 18.74 % than Sample B1.

Widening the notch width of narrow bandgap CIGSe absorber by highly excessive Cu deposition during growth

To further broaden the notch width and lower its minimum bandgap value, we have explored the use of excessive Cu during the deposition process. Although the application of the pre-CIGSe layer in the narrow

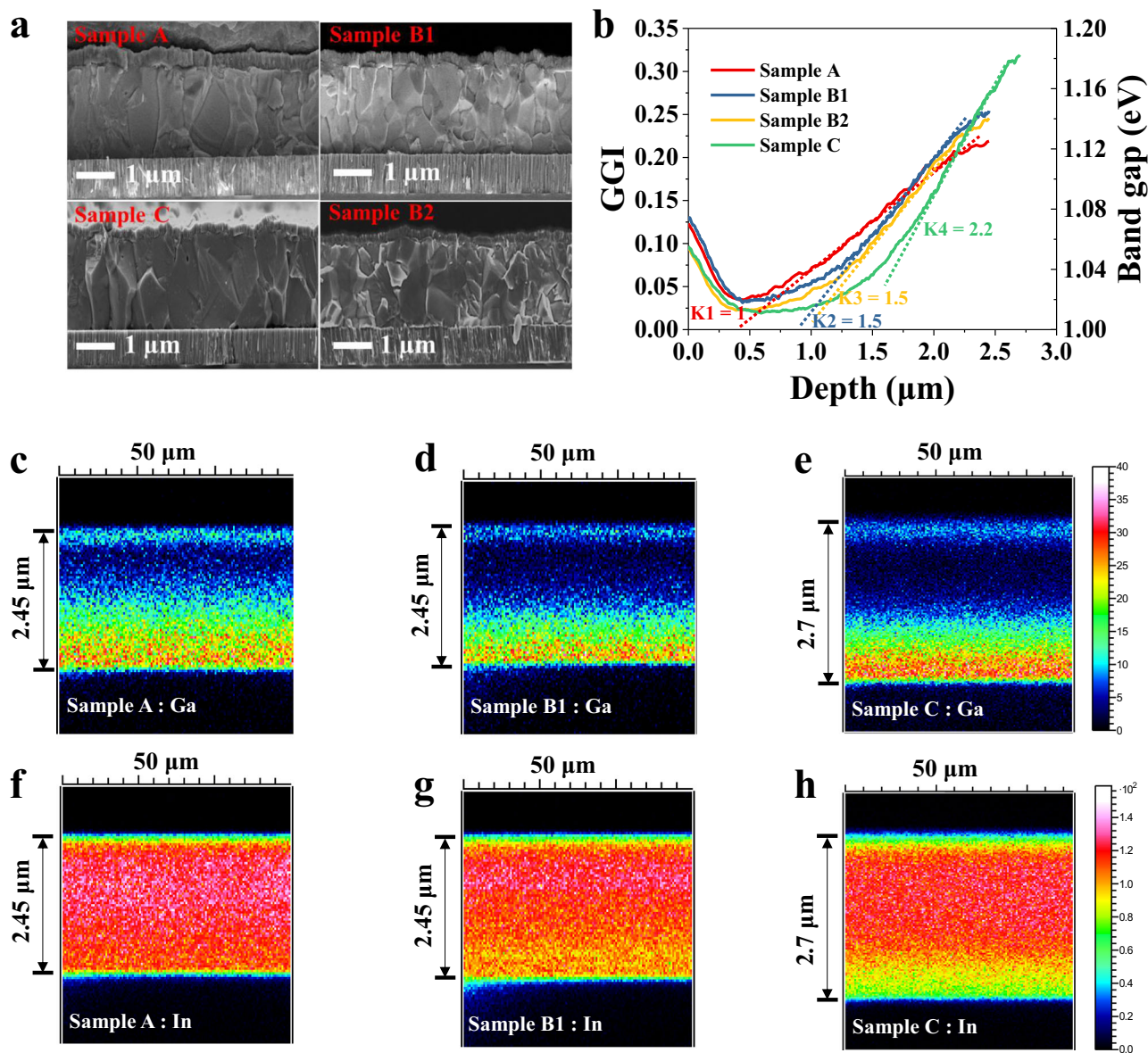


Fig. 3 | Characterizations of absorber layers by SEM and ToF-SIMS. **a** Cross-sectional SEM images of Sample A, B1, B2 and C prepared by different profiles. **b** Depth profiles of GGI calculated from ToF-SIMS data for the narrow bandgap CIGSe absorbers for Sample A, B1, B2 and C. The dashed lines are the eye-guided slopes of the back Ga grading. **c–e** ToF-SIMS element mapping of Ga for Sample A, B1 and C. **f–h** ToF-SIMS element mapping of In for Sample A, B1 and C. The depth direction is along the vertical axis.

Table 2 | Photovoltaic parameters of the solar cells for Sample A, B1, B2, C and C-RbF

Sample	ΔGGI	V_{OC} (mV)	J_{SC} (mA/cm ²)	FF (%)	PCE (%)	E_g (eV)	$V_{OC, def}$ (V)
A	0.18	601	39.21	75.64	17.82	1.03	0.429
B1	0.22	614	40.40	76.30	18.93	1.02	0.406
B2	0.22	601	41.40	75.28	18.74	1.01	0.409
C	0.30	620	41.46	75.77	19.47	1.01	0.390
C-RbF	0.30	642 (637)	41.70 (41.62)	76.06 (76.44)	20.37 (20.26)	1.01	0.368 (certified)

bandgap CIGSe absorber has already resulted in remarkable improvements in device performance compared to the traditional three-stage co-evaporation process, the minimum bandgap remains high as affected by the amount of Ga in the pre-CIGSe layer and the grains near the Mo surface remains small, as observed in Fig. 3a. These two shortcomings must be overcome in order to achieve better narrow

bandgap CIGSe devices. Excessive Cu deposition technique has usually been employed in CIGSe fabrication to improve the crystalline quality of absorber when the substrate temperature is relatively low³⁴ and/or when the overall GGI ratio is high^{35–37}. Further, the excessive Cu deposition technique can change the population of Cu vacancy and reduce the number of Ga_{Cu} and In_{Cu} antisites and thus

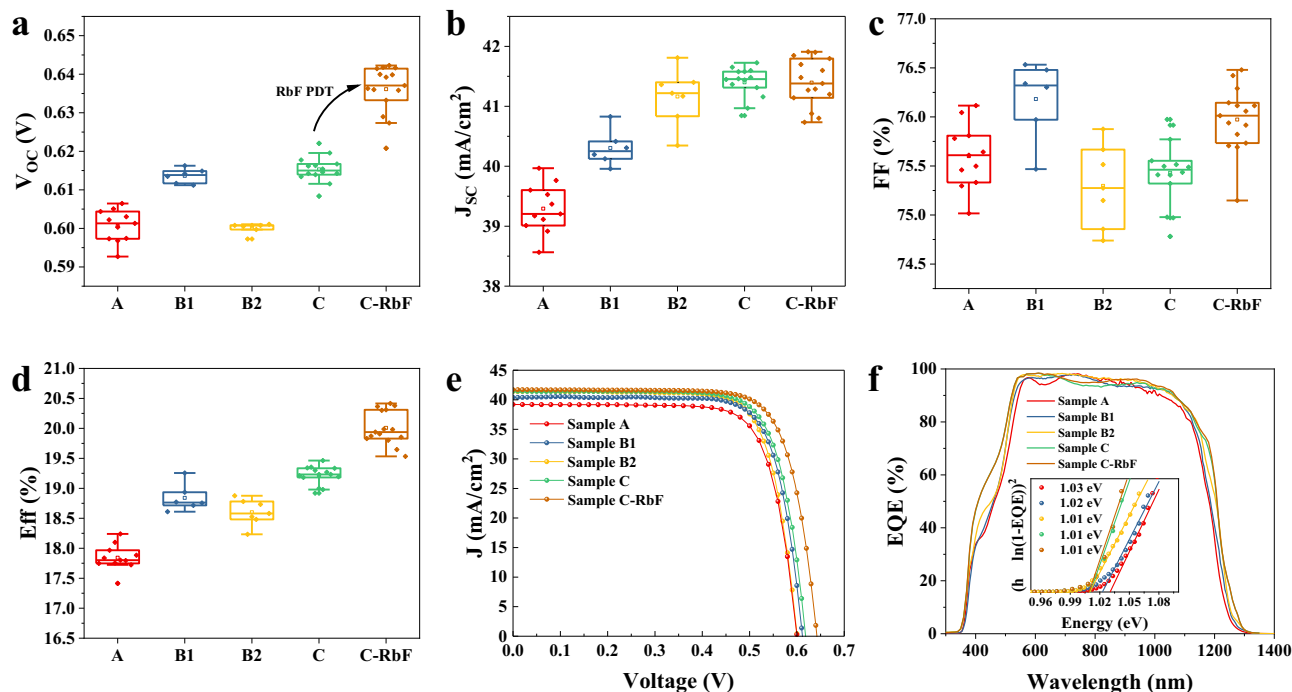


Fig. 4 | Device performance for different deposition profiles. a–d Statistical boxplot of V_{OC} (a), J_{SC} (b), FF (c), and Eff (d) for narrow bandgap CIGSe deposited by different profiles with or without RbF PDT. **e** Typical J - V curves and **(f)**, EQE spectra of CIGSe solar cells for comparison.

limit the inter-diffusion between In and Ga^{34,38–40}. Inspired by these ideas, we implemented it in the narrow bandgap CIGSe absorber and designed Profile C based on Profile B, as illustrated in Fig. 1c. In Profile C, the deposition of the pre-CIGSe layer and the deposition of In in the first stage remained the same as for Sample B1. The excessive Cu deposition was applied in the second stage, where 5% excessive Cu was deposited after reaching the stoichiometric point ($CGI=1$ at this point), followed by 15% In deposition at a slow deposition rate and another 10% Cu deposition at the normal deposition rate. The resulted CIGSe layer would retain the same CGI (~ 0.92) but increased thickness (see Supplementary Fig. 5 for absorber thickness optimization) when compared to Sample B1. This approach ensures the formation of large grain sizes while minimizing the generation of Cu_xSe phase. The optimization of Cu excess is demonstrated in Supplementary Fig. 6.

It is well-known that post-deposition treatment (PDT) by heavy alkali element doping with KF, RbF, or CsF can significantly improve the quality of the p-n junction for normal bandgap CIGSe absorbers^{41–45}. Here, we implemented the same treatment for narrow bandgap CIGSe absorbers. After completing the narrow bandgap CIGSe deposition process, Sample C with CGI composition of ~ 0.92 was subjected to RbF treatment (Sample C-RbF) at a substrate temperature of 280 °C for 20 min under Se atmosphere (Supplementary Fig. 7). For better comparison, the other absorbers without RbF post-deposition treatment were also post-annealed at the same substrate temperature of 280 °C in the Se-atmosphere for 20 minutes.

As shown in the cross-sectional SEM images (Fig. 3a), owing to the highly excessive Cu deposition, the grain size is remarkably increased and the film quality of the CIGSe absorbers is consequently improved. In Fig. 3b, the GGI depth profile also demonstrates a broadening of the notch region from 0.75 μm in Sample B2 to 0.90 μm in Sample C presently. More significantly, the slope of Ga back grading is further increased from 1.5 to 2.2 times of that in Sample A, benefitting from reduced inter-diffusion of Ga and In due to the reduced Cu vacancies with excessive Cu deposition.

The device performance results of these groups of solar cells are also depicted in Fig. 4a–f. The introduction of 15% excess copper during the CIGSe deposition process in Profile C leads to a further increase of $J_{SC} \sim 0.3$ mA/cm² compared to Sample B2 and a significant increase of $J_{SC} \sim 1.5$ mA/cm² compared to Sample B1 with the same amount of total Ga. This median value increase can be attributed to the excessive Cu deposited beyond the stoichiometry point, which facilitates the formation of a wide notch region with a nearly constant and lower GGI composition (Fig. 3b). The higher GGI value near the back interface and the steeper slope of Ga back grading for Sample C clearly contributes to the significant increase of $V_{OC} \sim 20$ mV compared to Sample B2 and a moderate increase of $V_{OC} \sim 5$ mV compared to Sample B1 that possessed the same amount of total Ga. The RbF PDT gives rise to Sample C-RbF with a further increase of V_{OC} by ~ 20 mV, FF by 0.5% in absolute, and a remarkable increase in PCE. Figure 4e, f and Table 2 illustrate the results of our typical-performing devices in each group, from which the best achieved PCE is 20.37% with a V_{OC} of 642 mV, FF of 76.06%, and J_{SC} of 41.70 mA/cm².

Defect analysis and mechanisms for the improved device performance

To investigate the origin of the absorber improvements, we probe the defect densities and their distributions. It is well known that there are two types of defects, N1 and N2, that exist in CIGS materials⁴⁶. Similar to other recent reports^{47–49}, only N1 exists in our high quality samples. As seen from Supplementary Fig. 8, there is only one type of traps observed in the admittance spectroscopic curves and the respective activation energy is found to be 79.6 meV for Sample A, 33.9 meV for Sample B1, and 27.1 meV for Sample C, close to the lower bound of N1 defects in literature^{48,50}. Fig. 5a as well as Supplementary Table 1 presents the defect density extracted from capacitance-voltage (C-V) (Supplementary Fig. 9) and drive-level capacitance profiling (DLCP) (Supplementary Fig. 10) measurements. Five representative samples CIGSe, FG-0, B1, C, C-RbF are compared. Since the C-V measurement involves both bulk defects and interface defects but the DLCP

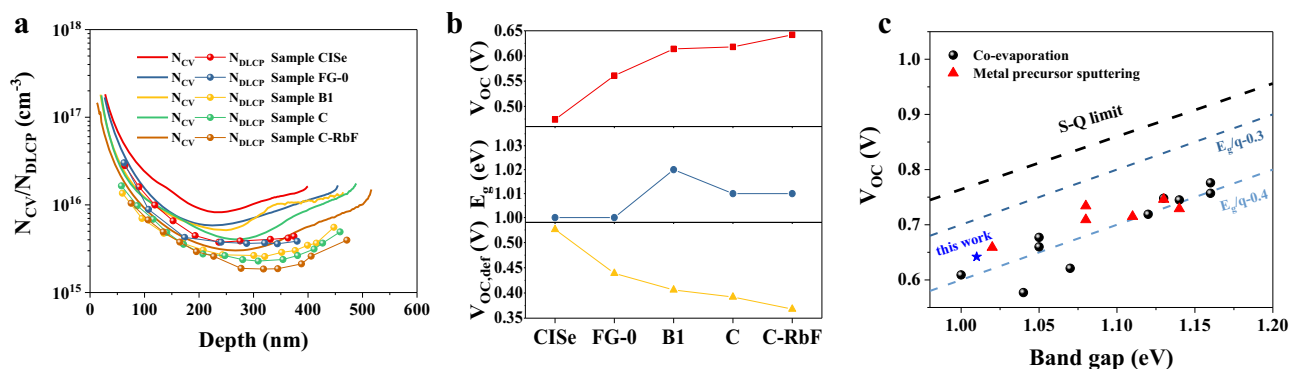


Fig. 5 | Defect analysis for V_{oc} improvement. **a** Defect density derived from the capacitance-voltage (C-V) and the drive level capacitance profiling (DLCP) measurements for samples ClSe, FG-0, B1, C, and C-RbF. **b** The variation of V_{oc} , E_g and

$V_{oc,def}$ for the corresponding ClSe solar cells. **c** Summary graph of V_{oc} with different E_g for typical ClSe solar cells. The device in this work is marked with a blue star.

measurement is only sensitive to bulk defects^{46,51–53}, the difference of these two effectively represents the contribution of interface defects. Taking the difference value as a representation of interface defect density, we would obtain an effective interface defect density around $5\text{--}6 \times 10^{15} \text{ cm}^{-3}$ for ClSe, FG-0, B1 and C, but a significantly reduced value of around $3.2 \times 10^{15} \text{ cm}^{-3}$ for Sample C-RbF, revealing that RbF post-deposition treatment has indeed substantially reduced the interface defect density. The depth distribution of N_{DLCP} exhibits an apparent high defect density in the near interface region for ClSe and FG-0, but about $2.0 \times 10^{15} \text{ cm}^{-3}$ lower defect density for the rest samples, most likely originating from the higher formation energy of Ga_{Cu} than In_{Cu} antisite defects³¹, demonstrating a benefit from front Ga incorporation^{54–56}. The presence of donor defects In_{Cu} and Ga_{Cu} has a negative impact on device performance⁵⁶, and might have a complicated pathway to contribute to the N1 type defects measured here. While reasonable acceptor-type atomic defect model of N1 defect has not been identified so far in the literature after many years' research, we speculate that the N1 defect may be associated with In_{Cu} and Ga_{Cu} defects, for which a detailed discussion is presented in Supplementary Fig. 11. As one gets deeper into the bulk, the Cu excess and RbF treatment respectively further reduce the bulk defect as anticipated, due to improvement of ClSe grain size and passivation of the grain boundaries.

Moreover, the incorporation of Ga and particularly the Cu excess adopted in the growth process can widen the space charge region (W_d), increasing the width from $267 \pm 6 \text{ nm}$ for ClSe, to $329 \pm 8 \text{ nm}$ for FG-0, to $360 \pm 10 \text{ nm}$ for B1, to $381 \pm 11 \text{ nm}$ for C, and to $390 \pm 11 \text{ nm}$ for C-RbF. This indicates that the densities of free carriers (hole in this case) and the ionizable defects are reduced, likely due to the suppressed V_{Cu} density. The increase of W_d further favors for carrier separation in the p-n junction region. The apparent trap density of the best ClSe solar cell is about $(2.12 \pm 0.10) \times 10^{15} \text{ cm}^{-3}$ in the bulk and about $(3.21 \pm 0.31) \times 10^{15} \text{ cm}^{-3}$ at the interface, both exhibiting lower values compared to other samples. These findings suggest that appropriate Ga back and front grading, optimized Cu excess strategy, and RbF treatment can subsequently increase the W_d and reduce bulk and interface defect densities, improving the photocarrier extraction and transport, and suppressing carrier recombination both in the junction and at the interface, leading to an open circuit voltage enhancement. Combined the results depicted in Figs. 2a, 4a, the V_{oc} value increases from $\sim 560 \text{ mV}$ to $\sim 600 \text{ mV}$ due to the Ga incorporation in the front portion of absorber with lowered defect density within the junction; further enhances to $\sim 620 \text{ mV}$ by Cu excess with reduction of defect density within the junction and in the bulk; and finally reaches $\sim 640 \text{ mV}$ by RbF PDT due to further reduction of defect density within the junction and particularly reduction of defect density at the

interface. In addition to the lower defect density, the V_{oc} increase by as much as $\sim 40 \text{ mV}$ by front Ga grading must also be attributed to the widened bandgap near the interface which can further suppress the carrier recombination rate via the Shockley-Read-Hall mechanism even the number of recombination center is unchanged³¹.

Figure 5b shows the variation of V_{oc} , E_g and $V_{oc,def}$ for samples ClSe, FG-0, B1, C, C-RbF with different growth conditions. By employing the pre-deposited ClSe layer, appropriate Ga front grading, excessive Cu, and RbF-PDT in the ClSe absorber, the C-RbF device increases its V_{oc} by approximately $\sim 80 \text{ mV}$, and reduces its $V_{oc,def}$ to 368 mV . Figure 5c provides a summary of the reported $V_{oc,def}$ for ClSe solar cells. Notably, our work has achieved a $V_{oc,def}$ as low as 368 mV , which is not only a good achievement for narrow bandgap ClSe solar cells but also for all ClSe with even higher bandgap values grown by co-evaporation method. While the most outstanding devices still show a V_{oc} close to the $E_g\text{--}0.4 \text{ eV}$ line, our data point is quite above this line and shows comparable $V_{oc,def}$ value with the world record devices grown with more sophisticated method.

Performance of champion ClSe device in tandems

For the best narrow bandgap ClSe solar cells at 1.01 eV , we have reached a certified record efficiency of 20.26% (Certified by Shanghai Institute of Microsystem and Information Technology (SIMIT), Chinese Academy of Science with $V_{oc} = 637 \text{ mV}$, $J_{sc} = 41.62 \text{ mA/cm}^2$, $FF = 76.44\%$, Supplementary Note 1). Compared to the previous record efficiency of 19.2% for single Ga-graded narrow bandgap ClSe with a bandgap of 1.00 eV (achieving a V_{oc} of 609 mV , an FF of 74.6%, a J_{sc} of 42.3 mA/cm^2)²⁴, our champion device demonstrates a 4.5% improvement in V_{oc} and a 2.5% enhancement in FF , although there is a slight reduction in J_{sc} by 1.6%. Combining this best cell with a wide bandgap (1.67 eV) perovskite solar cell (PSC) in a mechanically stacked tandem configuration, we have obtained a four-terminal tandem device with an overall efficiency of 29.02% as shown in Fig. 6. The transmittance spectra of the semitransparent PSC is also shown in Supplementary Fig. 12. To eliminate the loss due to reflection at the contacting interface between PSC and ClSe subcells, index matching material was applied for the overall efficiency measurement. The higher EQE values in contrast to that allowed by transmittance spectra of PSC filter measured in air were due to the elimination of reflection at the interfaces between PSC filter and ClSe subcells by index matching material (Supplementary Fig. 12).

The four-terminal tandem device with an efficiency of 29.02% is the second best among reported perovskite/ClSe tandem solar cells (Fig. 5d), mainly because of a lower PCE from the top PSC subcell. Nevertheless, our narrow bandgap ClSe bottom subcell has contributed 10.0% absolute efficiency, the highest within our best

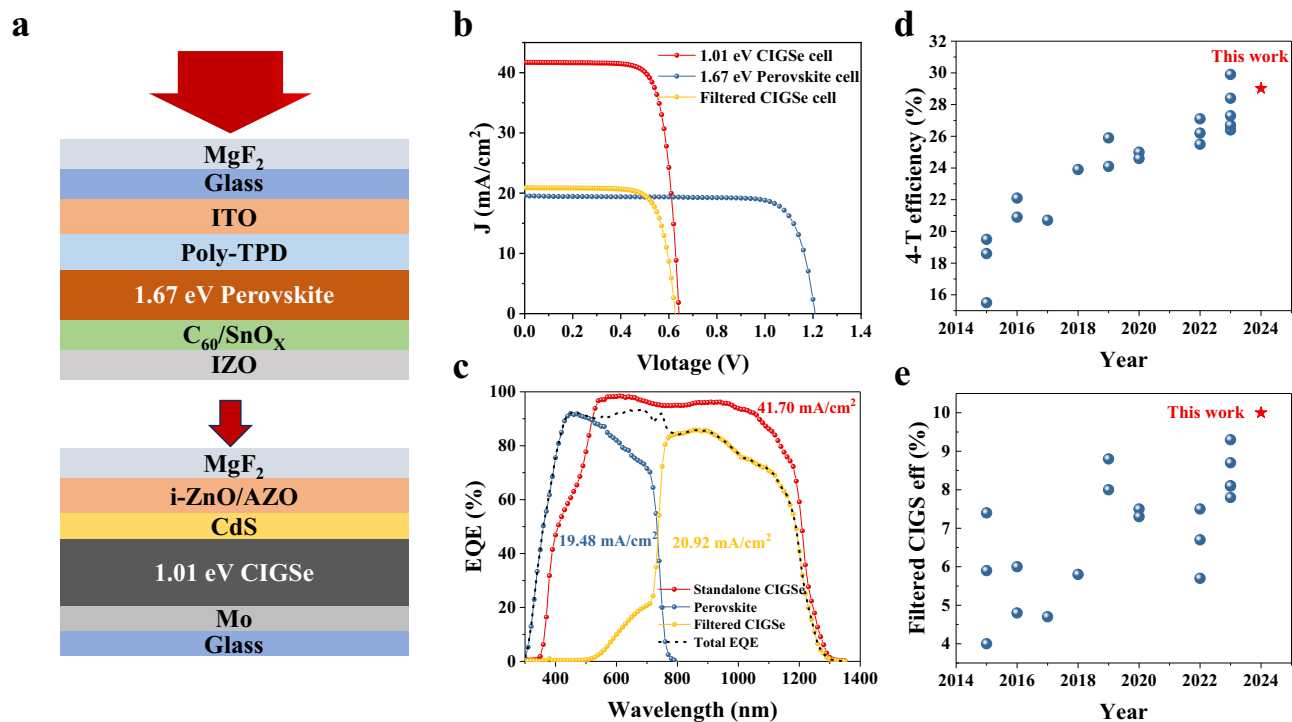


Fig. 6 | Performance demonstration in perovskite/CIGSe tandem cells.
a Schematic of the 4-T perovskite/CIGSe tandem cells. **b, c** J - V curves and EQE spectra of the standalone CIGSe cell, semitransparent perovskite top cell and filtered CIGSe cell. The total EQE is obtained by adding the EQE curves of the

perovskite top cell and the filtered CIGSe cell. **d, e** Summary of four-terminal perovskite/CIGSe tandem efficiency and filtered CIGSe efficiency in recent years surveyed from data listed in Supplementary Table 2.

knowledge (Fig. 6, Table 3 and Supplementary Table 2). Compared to our previous result with 9.3% contribution from a 1.04 eV bottom CIGSe sub-cell¹², the present enhancement is obvious. As also shown in Supplementary Table 2-4, our results can even be compared with the highest contribution from Si sub-cells. For all CIGSe and narrow bandgap perovskite bottom cells and most Si bottom cells in previous studies, their contribution to the overall efficiency of four-terminal tandems is below 10%, only in a few cases the Si bottom cells have made a contribution over 10% to the overall efficiency due to their higher standalone device PCE.

Discussion

A comment must be made to compare with previous best narrow bandgap CIGSe solar cells. The reported best narrow bandgap CIGSe absorber (19.2% PCE) was fabricated with single Ga back grading which used a high CGI of 0.96 in order to improve the bulk quality. Such high CGI would inevitably result in a secondary copper selenide (Cu_xSe) phase and require a surface etching normally by KCN ^{23,24,57–59}. Our absorber used a lower CGI (~ 0.92) and avoided the use of KCN .

Another comment can also be made to compare with narrow bandgap CIGSs solar cells which utilize sulfurization in the front surface of light absorber, resulting a back grading through Ga alloying and a front grading through S alloying. Such a CIGSs absorber

possesses a large back bandgap by raising the conduction band minimum via Ga alloying and a large front bandgap by lowering the valence band maximum via S alloying. Together with replacement of the commonly used CdS buffer layer by a combination of $Zn(O,S,OH)$ and $Zn_{0.8}Mg_{0.2}O$ layers using respectively chemical bath deposition (CBD) and atomic layer deposition (ALD), and replacement of the commonly used $ZnO:Al$ transparent conductive oxide layer by $ZnO:B$ using metal-organic chemical vapor deposition (MOCVD), a high PCE of 21.5% with a high V_{OC} of 659 mV and a particularly high $J_{sc} = 43.6$ mA/cm² due to a better UV-transparent buffer layer has been obtained at a minimum bandgap of 1.02 eV⁶⁰. Our present approach used traditional deposition procedures for the buffer layer and the transparent conduction oxide layer, in alignment with most of the present industrial practice.

In conclusion, we have demonstrated a combination of three stages of nanoscale control to fabricate a highly efficient narrow bandgap CIGSe solar cell with a bandgap only 10 meV larger than CIGSe. The introduction of a proper Ga front grading in CIGSe absorber greatly enhanced the V_{OC} by ~ 30 mV compared to devices with only Ga back grading. The employment of a pre-deposited high Ga content CIGSe layer prior to the traditional three-stage co-evaporation process suppressed the backside Ga diffusion to a good extent and increased the slope of the Ga back grading and enhanced the V_{OC} by ~ 10 mV. The adoption of 15% excess Cu in the growth process further reduced backside Ga diffusion, not only extending the notch region width but also maintaining a small minimum bandgap at 1.01 eV for the narrow bandgap CIGSe absorbers. The effect of these combined controls included improving crystalline quality and enabling the fabrication of desired U-shaped double Ga grading that was beneficial to the enhancement of spectral response in the infrared region. Through defect analysis, we have successfully identified the origins of V_{OC} increase for various Ga graded CIGSe absorbers, revealing the importance of Ga grading in carrier transport and extraction. Through the

Table 3 | The photovoltaic parameters of the best CIGSe standalone cell and 4-T perovskite/CIGSe tandem cells

	V_{OC} (V)	J_{sc} (mA/cm ²)	FF (%)	PCE (%)
CIGSe standalone (1.01 eV)	0.642	41.70	76.06	20.37
Perovskite cell (1.67 eV)	1.210	19.53	80.51	19.02
Filtered CIGSe	0.627	20.92	76.28	10.00
4-T PSC/CIGSe tandem				29.02

optimizations, we have achieved a champion device with an optical bandgap of 1.01 eV and a record low $V_{OC,def}$ of 368 mV, reaching a remarkable certified PCE of 20.26%, the highest reported efficiency for CIGSe solar cells with similar bandgaps. These advancements would pave the way for the development of CIGSe-based tandem solar cells.

Methods

CIGS device fabrication

The architecture of all CIGS solar cells consists of soda-lime-glass/Mo/CIGSe/CdS/i-ZnO/AZO/Ni-Al grid/MgF₂. Our optimization process focuses on the CIGSe absorber layer, while Profile A represents the conventional three stage co-evaporation process, Profile B represents the introduction of a pre-CIGSe layer with high Ga content and Profile C manipulates the excess Cu deposition in the 2nd stage. For the champion device, its absorber employed a pre-CIGSe layer, a front Ga grading, excessive Cu deposition, and RbF post deposition treatment (RbF-PDT). The RbF PDT was performed at a substrate temperature of 280 °C for 20 min, with the RbF source temperature set at 400 °C. All fabricated devices were finalized by incorporating a CdS buffer layer with a thickness of approximately 50 nm, achieved through chemical bath deposition. Subsequently, a 50 nm layer of i-ZnO and a 250 nm layer of 0.5 wt% Al:ZnO (AZO) were deposited onto the CdS layer using RF sputtering. Ni/Al metal grids and an additional MgF₂ antireflection layer (~110 nm) were deposited using electron beam evaporation. Unless otherwise specified, the size of solar cells was 0.5 cm² defined through mechanical scribing.

Characterizations

The current-voltage (*J*-*V*) curves were obtained using a Keithley 2400 source meter under standard test conditions at a temperature of 25 °C, with illumination provided by a 1000 W/m² AM 1.5 G light source from an HMI sun simulator (Enli Technology Co. Ltd., China). The output intensity of the light source was calibrated using the short-circuit current of a standard monocrystalline silicon (Si) solar cell from Fraunhofer ISE. The measurement was conducted from -0.1 to 0.8 V for CIGSe and from -0.1 to 1.3 V for PSC, both with step size of 0.01 V. In the tandem efficiency measurement, since the areas of the CIGSe and PSC are different, we used a large area perovskite filter that was produced identically as the small area PSC but without metallic electrodes to cover the CIGSe cell, as commonly used in other studies for four-terminal tandem cell measurement.

The external quantum efficiency (EQE) measurement was conducted using a QE/incident photon-to-electron conversion efficiency (IPCE) system (Enli Technology Co. Ltd., China). Here, a light spot of ~0.6 mm size was used and the EQE values were calibrated using a standard Si detector for short wavelength range (300 nm–1100 nm) and a Ge detector for long wavelength range (1100 nm–1400 nm), both of which were calibrated by Enli Tech Optoelectronic Calibration Lab. While all CIGS solar cells have Al grids for current collection in the *J*-*V* measurement, the light in the EQE measurement is shined between grid fingers which are separated by ~3 mm. In both *J*-*V* and EQE measurements, the electric contact is made by a metallic probe tip on a small Al pad that belongs to the Al grid to ensure the effective charge collection.

The GGI ([Ga]/([Ga]+[In])) and CGI ([Cu]/([Ga]+[In])) ratios were measured using an X-Ray Fluorescence Spectrometer (Skyscan Instrument, China). The compositional depth profile of the CIGSe films was detected using Time-of-Flight Secondary Ion Mass Spectrometry (ToF SIMS V, ION-TOF GmbH, Germany). We calibrated the In and Ga depth profiles obtained from ToF-SIMS by comparing the integrated In/Ga ratio with the ratio obtained from X-ray Fluorescence (XRF). Additionally, using calculated Ga composition dependent bandgap, we performed a second calibration by aligning the lowest point in the GGI depth distribution with the minimum bandgap value obtained from

EQE measurements. The two methods showed good agreement, enabling us to determine the true compositions of In and Ga.

The admittance spectroscopy was measured with TH 2828S (Tonghui, China), and operated from 100 Hz to 1 MHz at an AC voltage modulation of 50 mV under dark conditions in the temperature range of 100 K–260 K. The capacitance-voltage (C-V) and drive level capacitance profile (DLCP) were carried out on TH 2832 (Tonghui, China). The C-V plots were obtained at different DC bias from -0.8 to 0.8 V with a perturbation AC voltage of 50 mV under 100 kHz. The DLCP characteristics was measured at different DC bias from -0.6 to 0.6 V with a perturbation AC voltage from 20 to 200 mV under 100 kHz. The chosen frequency at 100 kHz ensures that the NI type defects can be completely ionized at room temperature (Supplementary Fig. 8).

Reporting summary

Further information on research design is available in the Nature Portfolio Reporting Summary linked to this article.

Data availability

Source data are provided with this paper. The main data supporting the findings of this study are available within the published article and its Supplementary Information and source data files. Additional data are available from the corresponding author on request. Source data are provided with this paper.

References

- Shockley, W. & Queisser, H. J. Detailed Balance Limit of Efficiency of p-n Junction Solar Cells. *J. Appl. Phys.* **32**, 510–519 (1961).
- Bremner, S. P., Levy, M. Y. & Honsberg, C. B. Analysis of tandem solar cell efficiencies under AM1.5G spectrum using a rapid flux calculation method. *Prog. Photovolt. Res. Appl.* **16**, 225–233 (2008).
- Li, H. & Zhang, W. Perovskite Tandem Solar Cells: From Fundamentals to Commercial Deployment. *Chem. Rev.* **120**, 9835–9950 (2020).
- Leijtens, T., Bush, K. A., Prasanna, R. & McGehee, M. D. Opportunities and challenges for tandem solar cells using metal halide perovskite semiconductors. *Nat. Energy* **3**, 828–838 (2018).
- Al-Ashouri, A. et al. Monolithic perovskite/silicon tandem solar cell with > 29% efficiency by enhanced hole extraction. *Science* **370**, 1300–1309 (2020).
- Chen, B. et al. Enhanced optical path and electron diffusion length enable high-efficiency perovskite tandems. *Nat. Commun.* **11**, 1257 (2020).
- Han, Q. F. et al. High-performance perovskite/Cu(In,Ga)Se₂ monolithic tandem solar cells. *Science* **361**, 904–908 (2018).
- Jošt, M. et al. Perovskite/CIGS Tandem Solar Cells: From Certified 24.2% toward 30% and Beyond. *ACS Energy Lett.* **7**, 1298–1307 (2022).
- Kim, D. H. et al. Bimolecular Additives Improve Wide-Band-Gap Perovskites for Efficient Tandem Solar Cells with CIGS. *Joule* **3**, 1734–1745 (2019).
- Lin, R. et al. All-perovskite tandem solar cells with improved grain surface passivation. *Nature* **603**, 73–78 (2022).
- Liu, J. et al. Efficient and stable perovskite-silicon tandem solar cells through contact displacement by MgF_x. *Science* **377**, 302–306 (2022).
- Liu, X. et al. Over 28% efficiency perovskite/Cu(In,Ga)Se₂ tandem solar cells: highly efficient sub-cells and their bandgap matching. *Energy Environ. Sci.* **16**, 5029–5042 (2023).
- Tong, J. et al. Carrier lifetimes of >1 μs in Sn-Pb perovskites enable efficient all-perovskite tandem solar cells. *Science* **364**, 475–479 (2019).
- Liang, H. et al. 29.9%-efficient, commercially viable perovskite/CuInSe₂ thin-film tandem solar cells. *Joule* **7**, 2859–2872 (2023).

15. Nakamura, M. et al. Cd-Free Cu(In,Ga)(Se,S)₂ Thin-Film Solar Cell With Record Efficiency of 23.35%. *IEEE J. Photovolt.* **9**, 1863–1867 (2019).
16. Keller, J. et al. High-concentration silver alloying and steep back-contact gallium grading enabling copper indium gallium selenide solar cell with 23.6% efficiency. *Nat. Energy* **9**, 467–478 (2024).
17. Jiang, Y. et al. High-Mobility In₂O₃:H Electrodes for Four-Terminal Perovskite/CuInSe₂ Tandem Solar Cells. *ACS Nano* **14**, 7502–7512 (2020).
18. Ruiz-Preciado, M. A. et al. Monolithic Two-Terminal Perovskite/CIS Tandem Solar Cells with Efficiency Approaching 25%. *ACS Energy Lett.* **7**, 2273–2281 (2022).
19. Jeong, C. et al. Examination of Suitable Bandgap Grading of Cu(In,Ga)Se₂ Bottom Absorber Layers for Tandem Cell Application. *Phys. status solidi (a)* **218**, 2000658 (2021).
20. Elanzeery, H. et al. High-performance low bandgap thin film solar cells for tandem applications. *Prog. Photovolt. Res. Appl.* **26**, 437–442 (2018).
21. AbuShama, J. et al. Improved performance in CuInSe₂ and Surface-modified CuGaSe₂ solar cells. *Conference Record of the 31th IEEE Photovoltaic Specialists Conference* **31**, 299–302 (2005).
22. Feurer, T. et al. Single-graded CIGS with narrow bandgap for tandem solar cells. *Sci. Technol. Adv. Mater.* **19**, 263–270 (2018).
23. Kamikawa, Y., Nishinaga, J., Shibata, H. & Ishizuka, S. Efficient Narrow Band Gap Cu(In,Ga)Se₂ Solar Cells with Flat Surface. *ACS Appl. Mater. Interfaces* **12**, 45485–45492 (2020).
24. Feurer, T. et al. Efficiency Improvement of Near-Stoichiometric CuInSe₂ Solar Cells for Application in Tandem Devices. *Adv. Energy Mater.* **9**, 1901428 (2019).
25. Feurer, T. et al. RbF post deposition treatment for narrow bandgap Cu(In,Ga)Se₂ solar cells. *Thin Solid Films* **670**, 34–40 (2019).
26. Hossain, M. I. et al. Perovskite/silicon tandem solar cells: from detailed balance limit calculations to photon management. *Nano Micro Lett.* **11**, 1–24 (2019).
27. Achard, V. et al. Study of Gallium Front Grading at Low Deposition Temperature on Polyimide Substrates and Impacts on the Solar Cell Properties. *IEEE J. Photovolt.* **8**, 1852–1857 (2018).
28. Kong, Y. et al. Formation of Ga double grading in submicron Cu(In,Ga)Se₂ solar cells by pre-depositing a CuGaSe₂ layer. *J. Mater. Chem. A* **8**, 9760–9767 (2020).
29. Kim, S. et al. Effect of Combined Alkali (KF + CsF) Post-Deposition Treatment on Cu(In,Ga)Se₂ Solar Cells. *Phys. status solidi (RRL) - Rapid Res. Lett.* **12**, 1800372 (2018).
30. Dongaonkar, S. et al. Universality of non-Ohmic shunt leakage in thin-film solar cells. *J. Appl. Phys.* **108**, 124509 (2010).
31. Kotipalli, R. et al. Influence of Ga/(Ga+In) grading on deep-defect states of Cu(In,Ga)Se₂ solar cells. *Phys. status solidi (RRL) - Rapid Res. Lett.* **9**, 157–160 (2015).
32. Chantana, J. et al. Impact of Urbach energy on open-circuit voltage deficit of thin-film solar cells. *Sol. Energy Mater. Sol. Cells* **210**, 110502 (2020).
33. Yang, S. C. et al. Influence of Ga back grading on voltage loss in low-temperature co-evaporated Cu(In,Ga)Se₂ thin film solar cells. *Prog. Photovolt. Res. Appl.* **29**, 630–637 (2021).
34. Carron, R. et al. Advanced Alkali Treatments for High-Efficiency Cu(In,Ga)Se₂ Solar Cells on Flexible Substrates. *Adv. Energy Mater.* **9**, 1900408 (2019).
35. Gong, J. B. et al. Over 11% Efficient CuGaSe₂ Solar Cells Without Using KCN Treatment. *Sol. RRL* **6**, 2200766 (2022).
36. Yang, S. H. et al. Bandgap optimization of submicron-thick Cu(In,Ga)Se₂ solar cells. *Prog. Photovolt. Res. Appl.* **23**, 1157–1163 (2015).
37. Szaniawski, P. et al. Influence of Varying Cu Content on Growth and Performance of Ga-Graded Cu(In,Ga)Se₂ Solar Cells. *IEEE J. Photovolt.* **5**, 1775–1782 (2015).
38. Avancini, E. et al. Impact of compositional grading and overall Cu deficiency on the near-infrared response in Cu(In,Ga)Se₂ solar cells. *Prog. Photovolt. Res. Appl.* **25**, 233–241 (2017).
39. Depredurand, V. et al. Current loss due to recombination in Cu-rich CuInSe₂ solar cells. *J. Appl. Phys.* **115**, 044503 (2014).
40. Ishizuka, S. et al. Group III Elemental Composition Dependence of RbF Postdeposition Treatment Effects on Cu(In,Ga)Se₂ Thin Films and Solar Cells. *J. Phys. Chem. C* **122**, 3809–3817 (2018).
41. Taguchi, N., Tanaka, S. & Ishizuka, S. Direct insights into RbInSe₂ formation at Cu(In,Ga)Se₂ thin film surface with RbF postdeposition treatment. *Appl. Phys. Lett.* **113**, 113903 (2018).
42. Kato, T. et al. Record Efficiency for Thin-Film Polycrystalline Solar Cells Up to 22.9% Achieved by Cs-Treated Cu(In,Ga)(Se,S)₂. *IEEE J. Photovolt.* **9**, 325–330 (2019).
43. Reinhard, P. et al. Alkali-Templated Surface Nanopatterning of Chalcogenide Thin Films: A Novel Approach Toward Solar Cells with Enhanced Efficiency. *Nano Lett.* **15**, 3334–3340 (2015).
44. Chirilă, A. et al. Potassium-induced surface modification of Cu(In,Ga)Se₂ thin films for high-efficiency solar cells. *Nat. Mater.* **12**, 1107–1111 (2013).
45. Jackson, P. et al. Effects of heavy alkali elements in Cu(In,Ga)Se₂ solar cells with efficiencies up to 22.6. *Phys. status solidi (RRL) - Rapid Res. Lett.* **10**, 583–586 (2016).
46. Heath, J. T., Cohen, J. D. & Shafarman, W. N. Bulk and metastable defects in CuIn_{1-x}Ga_xSe₂ thin films using drive-level capacitance profiling. *J. Appl. Phys.* **95**, 1000–1010 (2004).
47. Eisenbarth, T. et al. Interpretation of admittance, capacitance-voltage, and current-voltage signatures in Cu(In,Ga)Se₂ thin film solar cells. *J. Appl. Phys.* **107**, 034509 (2010).
48. Igalsen, M. & Czudek, A. Electrical spectroscopy methods for the characterization of defects in thin-film compound solar cells. *J. Appl. Phys.* **131**, 240901 (2022).
49. Schneider, T. et al. Comparison of Mo and ITO back contacts in CIGSe solar cells: Vanishing of the main capacitance step. *Prog. Photovolt. Res. Appl.* **30**, 191–202 (2022).
50. Cao, Q. et al. Defects in Cu(In,Ga)Se₂ chalcopyrite semiconductors: a comparative study of material properties, defect states, and photovoltaic performance. *Adv. Energy Mater.* **1**, 845–853 (2011).
51. Ni, Z. et al. Resolving spatial and energetic distributions of trap states in metal halide perovskite solar cells. *Science* **367**, 1352–1358 (2020).
52. Li, J. V. & Ferrari, G. *Capacitance spectroscopy of semiconductors Ch. 4* (CRC Press, New York, 2018).
53. Ravishanker, S., Unold, T. & Kirchartz, T. Comment on “Resolving spatial and energetic distributions of trap states in metal halide perovskite solar cells. *Science* **371**, eabd8014 (2021).
54. Jseng, Y.-Y., Chao, C.-J., Sung, H.-H. & Chen, T.-C. CIGS thin film and device performance produced through a variation Ga concentration during three-stage growth process. *Mater. Sci. Semicond. Process.* **87**, 162–166 (2018).
55. Wei, S.-H., Zhang, S. B. & Zunger, A. Effects of Ga addition to CuInSe₂ on its electronic structural and defect properties. *Appl. Phys. Lett.* **72**, 3199–3201 (1998).
56. Zhang, S. B., Wei, S.-H., Zunger, A. & Katayama-Yoshida, H. Defect physics of the CuInSe₂ chalcopyrite semiconductor. *Phys. Rev. B* **57**, 9642–9656 (1998).
57. Babbe, F. et al. Potassium fluoride postdeposition treatment with etching step on both Cu-rich and Cu-poor CuInSe₂ thin film solar cells. *Phys. Rev. Mater.* **2**, 105405 (2018).
58. Elanzeery, H. et al. Challenge in Cu-rich CuInSe₂ thin film solar cells: Defect caused by etching. *Phys. Rev. Mater.* **3**, 055403 (2019).
59. Hashimoto, Y. et al. Surface Characterization of Chemically Treated Cu(In,Ga)Se₂ Thin Films. *Jpn. J. Appl. Phys.* **35**, 4760 (1996).
60. Nakamura, M. et al. Perovskite/CIGS Spectral Splitting Double Junction Solar Cell with 28% Power Conversion Efficiency. *iScience* **23**, 101817 (2020).

Acknowledgements

This work was supported by the Special Fund for the “Dual Carbon” Science and Technology Innovation of Jiangsu province (Industrial Prospect and Key Technology Research Program, BE2022021 to X.X.), the National Natural Science Foundation of China (61904128 to J.G.), and the Knowledge Innovation Program of Wuhan-Shugung Project. The authors acknowledge the support from Wuhan University’s Start-up funding and the use of facilities and assistance at Wuhan University Analysis and Testing Center.

Author contributions

X.X. and J.G. directed and supervised the entire research. X.X., J.G., and J.Z. conceived the experiments, performed data analysis and wrote the paper. J.Z. led the fabrication and characterization of CIGSe solar cells. Z.M., Y.Z., and J.L. helped with the equipment maintenance and sample characterization. X.L. led the fabrication of perovskite solar cells. Q.L., G.F., and R.L. performed the CV and DLCP measurements. X.Z., W.L., and C.Y. contributed the admittance spectroscopy measurements. All authors discussed the results and commented on the paper.

Competing interests

The authors declare no competing interests.

Additional information

Supplementary information The online version contains supplementary material available at <https://doi.org/10.1038/s41467-024-54818-6>.

Correspondence and requests for materials should be addressed to Junbo Gong or Xudong Xiao.

Peer review information *Nature Communications* thanks Yousheng Wang, and the other, anonymous, reviewer(s) for their contribution to the peer review of this work. A peer review file is available.

Reprints and permissions information is available at <http://www.nature.com/reprints>

Publisher’s note Springer Nature remains neutral with regard to jurisdictional claims in published maps and institutional affiliations.

Open Access This article is licensed under a Creative Commons Attribution-NonCommercial-NoDerivatives 4.0 International License, which permits any non-commercial use, sharing, distribution and reproduction in any medium or format, as long as you give appropriate credit to the original author(s) and the source, provide a link to the Creative Commons licence, and indicate if you modified the licensed material. You do not have permission under this licence to share adapted material derived from this article or parts of it. The images or other third party material in this article are included in the article’s Creative Commons licence, unless indicated otherwise in a credit line to the material. If material is not included in the article’s Creative Commons licence and your intended use is not permitted by statutory regulation or exceeds the permitted use, you will need to obtain permission directly from the copyright holder. To view a copy of this licence, visit <http://creativecommons.org/licenses/by-nc-nd/4.0/>.

© The Author(s) 2024